CONF-8909235--2

CORRELATION OF WATERSIDE CORROSION AND CLADDING MICROSTRUCTURE IN HIGH–BURNUP FUEL AND GADOLINIA RODS*

H. M. Chung

Materials and Components Technology Division
Argonne National Laboratory
Argonne, Illinois 60439 USA

CONF-8909235--2

DE90 001439

September 1989

The submitted manuscript has been authored by a contractor of the U. S. Government under contract No. W-31-109-ENG-38. Accordingly, the U. S. Government retains a nonexclusive, royalty-free license to publish or reproduce the published form of this contribution, or allow others to do so, for U. S. Government purposes.

DISCLAIMER

This report was prepared as an account of work sponsored by an agency of the United States Government. Neither the United States Government nor any agency thereof, nor any of their employees, makes any warranty, express or implied, or assumes any legal liability or responsibility for the accuracy, completeness, or usefulness of any information, apparatus, product, or process disclosed, or represents that its use would not infringe privately owned rights. Reference herein to any specific commercial product, process, or service by trade name, trademark, manufacturer, or otherwise does not necessarily constitute or imply its endorsement, recommendation, or favoring by the United States Government or any agency thereof. The views and opinions of authors expressed herein do not necessarily state or reflect those of the United States Government or any agency thereof.

INVITED PAPER for presentation at the International Atomic Energy Agency Technical Committee Meeting on "Fundamental Aspects of Corrosion of Zirconium–Base Alloys in Water Reactor Environments," Sept. 11–15, 1989, Portland, OR.

---

*Work supported by the U. S. Department of Energy, under contract W–31–109–Eng–38.

MASTER

DISTRIBUTION OF THIS DOCUMENT IS UNLIMITED

CORRELATION OF WATERSIDE CORROSION AND CLADDING MICROSTRUCTURE IN HIGH–BURNUP FUEL AND GADOLINIA RODS

H. M. Chung

Materials and Components Technology Division
Argonne National Laboratory
Argonne, Illinois 60439 USA

ABSTRACT

Waterside corrosion of the Zircaloy cladding has been examined in high–burnup fuel rods from several BWRs and PWRs, as well as in 3 wt% gadolinia burnable poison rods obtained from a BWR. The corrosion behavior of the high–burnup rods was then correlated with results from a microstructural characterization of the cladding by optical, scanning–electron, and transmission–electron microscopy (OM, SEM, and TEM). OM and SEM examination of the BWR fuel cladding showed both uniform and nodular oxide layers 2 to 45 µm in thickness after burnups of 11 to 30 MWd/kgU. For one of the BWRs, which was operated at 307°C rather than the normal 288°C, a relatively thick (50 to 70 µm) uniform oxide, rather than nodular oxides, was observed after a burnup of 27 to 30 MWD/kgU. TEM characterization revealed a number of microstructural features that occurred in association with the intermetallic precipitates in the cladding metal, apparently as a result of irradiation–induced or –enhanced processes, i.e., (1) partial amorphization of large Zr–Fe–Cr and Zr–Fe–Ni precipitates (300 to 800 nm in size), (2) virtually complete amorphization of small intermetallic precipitates and subsequent dissolution of the alloying elements, and (3) spinodal–like fluctuation and redistribution of the alloying elements following the amorphization and dissolution. The BWR rods that exhibited white nodular oxides contained large precipitates (300 to 700 nm in size) that were partially amorphized during service, indicating that a distribution of the large intermetallic precipitates is conducive to nodular oxidation. However, for a similar size and distribution, relatively thick uniform oxides, rather than nodular oxides, were produced in the BWR rods irradiated at 307°C. This indicates that the nodular oxidation is strongly influenced by the reactor operating temperature as well as by the size and distribution of the intermetallic precipitates.

Besides the microstructural features associated with the intermetallic precipitates, TEM stereo electron microscopy revealed microscopic zirconium hydrides (30 to 100 nm in size) that were too small to be resolved by OM or SEM. Stereoscopic examination revealed a tendency for precipitation of the microscopic hydrides with c–component dislocations as the burnup increased. Also, an examination of bright– and dark–field stereopair images revealed three–dimensional distributions of fine cubic–zirconium–oxide precipitates (5 to 10 nm in size) and unidentified "black–dot" (5 to 10 nm) and "white–dot" defects (3 to 10 nm) in the cladding metal. In the BWR gadolinia rods, an unidentified phase of light contrast and ~50 nm in size was also observed. However, there was no evidence to suggest that either the hydrides or the cubic oxide particles were directly associated with waterside corrosion (i.e., that they promote nodular oxidation). It seems that the combined effects of fuel cladding operating temperature and the fabrication–induced size and distribution of intermetallic precipitates are the primary factors that influence the nature and morphology of the oxides.

1. INTRODUCTION

It has been well established that the corrosion behavior of unirradiated Zircaloy–2 and –4 is strongly influenced by the microstructure and microchemistry of the cladding metal, in particular, size, density, and chemical compositions of the intermetallic precipitates and concomitant microchemical variations that are associated with the precipitation of the intermetallics. In recent years, investigation of similar influences has been conducted for irradiated Zircaloys in a number of laboratories in association with extended–burnup fuel development. Structural transformation of the $Zr(Fe,Cr)_2$ and $Zr_2(Fe,Ni)$ precipitates in irradiated Zircaloys has been investigated in a number of recent papers.[1–6] In general, irradiation has been observed to induce amorphization and dissolution of these precipitates and modifies the size, number density, and compositions of the precipitates as well as the surrounding Zircaloy matrix. The microstructural modification appears to be sensitive to irradiation temperature; both size and density decrease with increased neutron fluence at 290–300°C, but the average size increases with fluence at 340–390°C.[5] The microstructural modification could have an influence on corrosion properties either because of the redistribution of the existing precipitates, or because of secondary precipitation from the matrix, or because of an increase or decrease of interstitial and substitutional solutes. Besides the $Zr(Fe,Cr)_2$ and $Zr_2(Fe,Ni)$, other forms of intermetallic precipitates, $Zr_3(Fe,Cr)_2$,[7] $Zr(Fe,Cr)_3$,[7] and Zr_3Fe,[5,8] have been reported for unirradiated Zircaloys. Precipitates rich in Sn,[9] zirconium silicide Zr_3Si,[2,10] and sulfides of Zr–Cu have also been reported for irradiated Zircaloys.

Besides these intermetallic precipitates, nonmetallic precipitates in bulk irradiated Zircaloys have been reported from TEM stereo examination of high–burnup fuel cladding, i.e., cubic–ZrO_2 particles 5–10 nm in size[5,10] and small (30–100 nm in size) δ–hydrides,[10] which could not be resolved by optical or scanning–electron microscopies. In addition to the usual "black–dot" defects, ≤10 nm in size, "white–dot" defects of similar size have also been reported[10] in irradiated specimens, indicating a possibility of either microvoids or fine secondary precipitates containing metallic elements lighter than Zr. From this review, it is evident that no consensus among investigators has been reached yet on precipitate identification or even the existence of certain precipitates, in particular for irradiated materials.

The size[11,12] and crystalline structure[11] of the intermetallic precipitates $Zr(Fe,Cr)_2$ and $Zr_2(Fe,Ni)$ have been correlated with waterside corrosion of BWR[11,12] and PWR[12] fuel cladding in two recent investigations. Results of these studies indicated an increased BWR corrosion rate for cladding containing larger intermetallic precipitates. However, an opposite trend has been observed for PWR corrosion.[12] While the size effects appear consistent with out–of–reactor corrosion behavior, the opposite trend for BWR and PWR environments has not been understood at present. In this investigation, waterside corrosion of fuel and absorber rods from several BWRs and PWRs has been examined after a burnup of 11–30 MWd/kgU. Precipitates and other microstructural characteristics of the rods have also been examined by TEM stereomicroscopy to provide a better understanding of the irradiation–induced structural modification, and an attempt has been made to correlate the microstructural and corrosion characteristics.

2. EXPERIMENTAL PROCEDURES

Spent–fuel rods from three operating BWRs and one PWR as well as absorber rods containing UO_2–3 wt.% Gd_2O_3 fuel from one BWR was obtained. The fuel burnup and neutron fluence were in the range of 11–30 MWd/kgU and 1.6 to 4.4 x 10^{21} ncm^{-2} (E > 0.1 MeV), respectively. Waterside oxide morphology and layer thickness have been examined from polished and etched metallographic specimens of defueled rod sections of each reactor. The results are summarized in Table 1. Before the rod sections were cut, eddy–current inspection was conducted to ensure that no defects in cladding existed. All the rods were free from defects except the gadolinia absorber rod from BWR–D. The gadolinia rod showed indications of pin–hole pellet–cladding interaction (PCI) failure. A metallographic section for the gadolinia rod was then cut right from the axial location of the pin–hole failure. Subsequent examination of SEM fractography showed that the failure was indeed a PCI failure.[13] Cladding from some of the BWRs was annealed and recrystallized as shown in Table 1. The TEM disks were jet–thinned in electrolyte solutions of perchloric acid, butylcellosolve, and methanol (volume ratio 2:12:30) maintained at –70°C. The foil plane of the TEM specimen was nearly perpendicular to the cladding radial direction. The thin–foil specimens were then examined in a JEOL CX–II STEM or in a Kratos/AEI–EM7 HVEM, which were operated at 0.1 and 1 MeV, respectively. The latter, equipped with a double–tilt hot stage, has a demonstrated lattice resolution of 0.35 nm. The diffraction patterns obtained from the HVEM were more accurate than those from conventional microscopes. The camera lengths of the microscopes were calibrated independently. Reflections from the Zr–matrix were used as standards to find an exact camera length for each diffraction pattern.

3. RESULTS

3.1 Oxide Morphology and Thickness

Oxide morphology and thicknesses of the fuel and absorber rods from the five reactors are shown in Fig. 1 and summarized in Table 1, respectively. Fuel rods from the BWR–A and –C showed nodular oxides with maximum local thickness up to ~45 μm after burnup of ~14 MWd/kgU. Other fuel and the absorber rods showed uniform waterside corrosion layers. The uniform oxide layer of BWR–B was relatively thicker, i.e., 50–70 μm after burnup of ~30 MWd/kgU. Compared to the normal operating temperature of 288°C of the other BWRs, BWR–B was operated at a higher temperature of 307°C. The higher temperature is believed to be a significant factor of the higher oxidation. The waterside oxidation of the gadolinia rods of BWR–D was minimal (oxide layer 5–9 μm thick after 24 MWd/kgU), reflecting relatively lower operating temperature of ~240°C. However, corrosion layer thickness on the inner surface of the gadolinia rod cladding was significantly larger than the UO_2 rods.

3.2 Intermetallic Precipitates

Only two types of intermetallic precipitates containing Fe,Cr or Fe,Ni were identified, i.e., $Zr(Fe,Zr)_2$ and Zr_2 (Fe,Ni). Examples of TEM morphology and indexed selected–area diffraction (SAD) patterns of the hexagonal $Zr(Fe,Cr)_2$ (lattice constant a = 0.504 nm, c = 0.816 nm), and tetragonal $Zr_2(Fe,Ni)$ (a = 0.651 nm, c = 0.541 nm) are shown in Fig. 2. After a neutron fluence of 3.3×10^{21} ncm^{-2} (E >0.1 MeV), both precipitates were partially amorphized to a significant extent at the peripheries. The peripheral amorphization and dissolution of Fe, Cr, and Ni could be readily detected from comparison of bright– and dark–field image contrasts. No cubic modification of $Zr(Fe,Cr)_2$ precipitates were observed either in Zircaloy–2 or –4, confirming a previous report.[2] Relatively large precipitates on the order of several hundred nanometer are shown in Fig. 3 for other BWR fuel and gadolinia rods. The range of precipitate size for the BWR cladding is summarized in Table 1.

In the PWR–A cladding (fluence 4.4 x 10^{21} ncm^{-2}), it was difficult to find intermetallic precipitates $Zr(Fe,Cr)_2$ that were still in crystalline form. It appeared that only a few oversize $Zr(Fe,Cr)_2$ precipitates survived the irradiation–induced amorphization and most of the smaller ones were fully amorphized and dissolved in the matrix. Typically, small holes (Fig. 4A) were observed in the electron–transparent region of the TEM specimens of the PWR–A. Apparently, the holes were formed because of preferential localized corrosion attack during jet–thinning process of the TEM specimen near the amorphized and dissolved $Zr(Fe,Cr)_2$ precipitates. Such holes were usually surrounded by amorphous regions 5–20 times larger than the size of the precipitates (Figs. 4B and 4C). It appeared that the irradiation–induced amorphization and dissolution for a similar level of fluence are more extensive in PWR than in BWR cladding, probably reflecting effects of higher neutron flux or temperature of the PWR fuel rods, or both. In limited local regions, the amorphization and dissolution appeared fully advanced, resulting in local supersaturation of Fe and Cr. In those regions, irradiation–induced spinodal–like fluctuation of solute atoms was manifested by alternating light and dark contrasts of several hundred nanometer wavelength, as shown in the bright–field image of Fig. 5. Size of the intermetallics in the PWR cladding was deduced to be 40–100 nm from examination of high–magnification bright– and dark–field images similar to Fig. 4B.

3.3 Zr_3Si Precipitates

Zirconium silicides were present in minor amounts in the PWR spent–fuel cladding. An example of the silicides is shown in Fig. 6. SAD patterns of several different zones of the precipitate were obtained through a tilting experiment. The analysis of the SAD patterns showed the precipitate to be the tetragonal (a = 1.101 nm, c = 0.545 nm) Zr_3Si phase.

3.4 δ Hydrides

TEM specimens, sectioned from regions adjacent to the metallographic mount shown in Fig. 1 for the BWR gadolinia rod, exhibited distinctively complex microstructural characteristics. Typical examples of bright–field images of the region are shown in Fig. 7A. In the figure, a pair of stereomicrographs, obtained by ~10° tilting of the gadolinia–rod specimen, are shown. Corresponding SAD patterns are shown in Fig. 7B. Analysis of the SAD patterns showed reflections from δ hydrides and cubic–ZrO_2 phases in addition to those from surface antifact hydrides denoted by "χ" letters in the SAD patterns. The δ hydrides are shown in Fig. 7A by nearly spherical or elliptical dark lumps 30–100 nm in size. Also visible in the figure are nearly spherical lumps of light contrast within the grain and nearly continuous strips of light contrast at the grain boundary. These regions of light contrast could not be identified; however, the contrast indicates that the regions are rich in elements (e.g., Fe, Cr, and Ni) lighter than the Zr matrix. They could also be secondary phases, voids, or cavities. Similar regions of light contrast have been also reported previously for Zircaloy–4 specimens irradiated to a fluence of 5 to 7 x 10^{21} ncm^{-2} (E >1 MeV) at 381 to 445°C.[14]

The hydrides shown in Figs. 7A and 7B are not the same as the long δ–hydride stringers (~50 nm wide and ~1000 nm long) that can be readily resolved metallographically in most of the irradiated or hydrided Zr alloys. To resolve the nature of the smaller δ hydrides of Fig. 7A (i.e., bulk or surface nature), a stereo-view examination of the bright–field image has been conducted. In Fig. 7C, 75 images of the dark hydrides and light–contrasted regions (either cavities or secondary phase rich in alloying elements) were selected and examined with a Cartographic Engineering Ltd. mirror stereoscope. Thirty images on or near the top surface, 27 images in the middle of the specimen, and 18 on or near the bottom surface have been identified and marked in Fig. 7C with black triangles, circles, and squares, respectively. For instance, Images B, D, and E are located near the top surface. Images C, F, A, and G are located approximately 56, 65, 122, and 141 nm below Images B, D, and E. Relative depth of the images was determined from the equation

$$t = \frac{P}{2M \sin \theta} ,$$

where t = relative depth, P = parallax measured from stereoscope, M = magnification, and θ = tilt angle. Measurement of the relative depths from the top surface (e.g., between B and C) or from the bottom surface (e.g., between F and G) is facilitated by switching the stereopair left and right under the stereoscope.

The result of Fig. 7C shows that the dark hydride and the white dots and lumps are distributed in the bulk of the film that is ~140 to 145 nm in thickness. A careful examination of the bright–field images at higher magnifications shows a large number of void–like "white dots" ~3 nm in size distributed in most regions of Fig. 7A. Also visible in the bright–field images are "black–dot" defects ~3 nm in size. When the small "white–dots" contrast are superposed on the dark hydride images, characteristic "strawberry–like" morphologies are visible, for example, Images 2 and 5.

3.5 Cubic ZrO_2 Precipitates

Evidence for the bulk nature of the cubic–ZrO_2 particles cannot be obtained from the bright–field stereopairs since the fine cubic–ZrO_2 particles were usually invisible in the bright–field. therefore, extensive tilt experiments were conducted to obtain dark–field stereopairs of good quality. Tilt angles of 5 to 12° for image magnifications of 30 to 50 thousand times were tried. The dark–field stereopair of Fig. 7D was obtained from the $(\bar{1}1\bar{1})$ reflections from the cubic–ZrO_2 phase, which is shown in the SAD patterns of Fig. 7B. Detailed examination of the dark–field stereopair clearly showed bulk nature of the cubic–ZrO_2 particles, which are distributed more or less uniformly through the specimen thickness. To show the bulk distribution to a reader in a more direct manner, 30 particles were selected in Fig. 7D from a stereoview of the dark–field pair. In identifying the matching particles in the stereopair, great care should be exercised since all the particles are not visible in both micrographs. The diffraction conditions are not identical in both micrographs of Fig. 7D. Relative depth of the particles selected in Fig. 7D was determined from parallax measurement and plotted in Fig. 7E. The result shows a more or less random distribution of the cubic–ZrO_2 particles through the thin–film specimen ~160 nm in thickness. The film thickness measured in Figs. 7B and 7E (i.e., 141 versus 160 nm) is in good agreement.

The small δ hydrides and cubic–ZrO_2 precipitates, similar to those of Fig. 7, were also observed in the fuel cladding of BWR–B and PWR–A, although density was somewhat less. In a recent study of Ref. 5, the cubic–ZrO_2 precipitates were reported to have been observed in all the irradiated specimens examined (fluence 5 to 17 x 10^{21} ncm^{-2}) but not in a specimen irradiated and subsequently annealed at 550°C for 48 h.

3.6 c–Component Dislocations

Hydrides similar to those of Fig. 7, but elongated perpendicular to [0002] direction, were frequently observed in high–fluence specimens in association with c–component dislocations. This is shown in Fig. 8. The dark–field image of Fig. 8 was obtained from (0002) reflection of Zr which is nearly superimposed on (002) of the cubic–ZrO_2 and (111) of the δ hydride. A stereoview examination of both dark–field (such as Fig. 8) and bright–field images showed that the elongated δ hydrides are also bulk phases precipitated in association with the c-component dislocations.

3.7 "Black–Dot" and "White–Dot" Defects

The "black–dot" defects were observed in all the irradiated specimens examined. However, the "white–dot" defects were observed only in some regions of the BWR–D gadolinia and PWR–A fuel rod cladding. Although very difficult, stereoview of the "black–" and "white–dot" defects could be obtained from high–magnification bright–field images, indicating that they are both bulk defects. It is tempting to attribute the "white–dot" defects as microvoids;[14] however, one cannot rule out the possibility of unidentified secondary precipitation.

4. DISCUSSION

It is evident that, as the fluence is increased, the $Zr(Fe,Cr)_2$ and $Zr_2(Fe,Ni)$ precipitates undergo a series of microstructural evolution, i.e., amorphization, dissolution, and irradiation–induced spinodal–like fluctuation of the dissolved alloying elements in an extreme case. Clear evidence of secondary precipitation was not observed, except the possibility that the "white–dot" defects and light–contrast lumps (such as those in Fig. 7A) may indeed be a secondary phase. However, distinct diffraction spots (e.g., those expected for Fe– or Sn–rich phases) were not observed. The occurrence of the nodular oxides in BWRs could be best correlated with the average size of the intermetallic precipitates (size before amorphization and dissolution) except for the BWR–B. It seems evident that the larger the average size, the possibility of nodular oxide formation is larger. This observation is consistent with results of other out–of–reactor investigations. Although it was difficult to quantify true corrosion rates because of variations in service temperature, burnup, and operating histories, oxidation was relatively heavier for cladding with larger precipitate size.

In the case of the BWR–B, thick (50–70 µm) uniform oxide layer instead of nodular oxide was formed despite the large size of intermetallic precipitates. This is attributed to a higher cladding service temperature that is associated with the higher coolant outlet temperature (i.e., 307 vs 288°C). That is, for the BWR environment, nodular oxide formation appears strongly dependent not only on the intermetallic precipitate size, but also on the fuel operating temperature. This is shown schematically in Fig. 9. In the figure, expected regions for uniform and nodular oxide formation are illustrated schematically as a function of cladding operating temperature and average precipitate size.

Waterside corrosion of the UO_2–3% Gd_2O_3 rods of BWR–D was very small (oxide 5–9 µm) after a three–cycle burnup of 24 MWd/kgU. This is apparently because of the lower operating temperature of the gadolinia absorber rods compared to fuel rods (i.e., ~240 vs 288°C). The gadolinia rods were unpressurized. This factor as well as the larger swelling and expansion usually associated with gadolinia–containing fuel pellets probably caused a tight contact between the cladding inner surface and the pellets, resulting in a significant clad ID corrosion (Fig. 1). It is also possible that excessive moisture may have been contained in the UO_2–Gd_2O_3 pellets, resulting in more ID oxidation (than UO_2 rods) and more hydrogen uptake in the cladding.

It should be emphasized that, although the stereomicroscopy demonstration of the bulk nature of the small hydrides and cubic–ZrO_2 particles was reported for the gadolinia–rod specimen, similar precipitates were also observed in other high–burnup fuel claddings, i.e., BWR–B and PWR–A. It appears that local variation in the number density of the bulk small hydrides and cubic–ZrO_2 precipitates is significant even in the same cladding section. In particular, density of the cubic–ZrO_2 precipitates appeared to be associated with high fluence and high oxygen content dissolved in the irradiated cladding metal.[15] Reduced ductility and, in some cases, even brittle–type fracture were reported previously in association with high density cubic–ZrO_2 precipitates and the δ hydrides.[15] In general, this situation is likely to develop in an extended–burnup fuel cladding metal underneath a thick oxide layer. This will in effect embrittle the local metal at the metal–oxide boundary, and, as a result, facilitate cracking along the boundary under the stress that is generated by the oxide formation. That is, the repeating self–cracking process which is usually associated with porous breakaway oxide growth is likely to be more pronounced and continuous along the boundary. There is evidence in the literature that oxidation rate "breaks away" after an oxide thickness of ~15 to 20 μm is reached.[16,17] When oxide films exceed this 15 to 20 μm critical thickness, they appear to develop an independent internal water chemistry, even with high hydrogen concentrations in the coolant, leading to a situation whereby both high corrosion rates and high hydrogen uptake rates can occur simultaneously. According to this "thick–film" hypothesis, the corrosion rates would then become less dependent on the bulk water chemistry outside the oxide as the oxide films became thicker. For fuel rod axial level of maximum temperature and maximum oxidation (i.e., approximately upper three–quarters level), the critical thickness of 15 to 20 μm is reached well before a burnup of ~25 MWd/kg. Oxide thickness measurements recently conducted for the maximum–oxidation level by KWU,[18] Framatome,[19] B&W,[20] C–E,[21] and Westinghouse[22] for extended–burnup (up to ~55 MWd/kg) fuel show thicknesses as high as 80 μm, well beyond the "thick–film" threshold. In this range of oxide thicknesses, observations have been reported which indicate that the oxidation at burnups ≥ 50 MWd/kg was larger than that extrapolated from the lower–burnup data at ≲40 MWd/kg. Thus, another type of acceleration of oxidation is indicated for extended–burnup >50 MWd/kg. The irradiation enhancement factor for in–reactor oxidation also appears to increase at burnups >50 MWd/kg.[18] Thick oxide layers produced in extended–burnup fuel rods show frequently long cracks near the metal–oxide boundary that are continuous and parallel to the metal–oxide boundary,[5,20,23] indicating a more pronounced separation along the boundary during the extended–burnup service.

5. CONCLUSION

1. Microstructural characteristics of commercial Zircaloy–2 and –4 claddings of fuel and gadolinia rods, obtained from several BWRs and a PWR after burnup of 11–30 MWd/kgU, have been examined by TEM stereomicroscopy. Besides the normal intermetallic precipitates $Zr(Fe,Cr)_2$ and $Zr_2(Fe,Ni)$, Zr_3Si precipitates, small δ hydrides (30–100 nm), cubic–ZrO_2 precipitates (5–10 nm), "black–dot" defects, and unidentified "white–dots" (<10 nm) and cavity–like lumps (50–100 nm) and grain–boundary features were observed. For high fluence level, spinodal–like fluctuation of alloying elements, apparently induced by irradiation, was also observed.

2. Out of these microstructural characteristics, occurrence of nodular oxidation in BWRs could be best correlated with a combined effect of average size of the intermetallic precipitates and cladding operating temperature. For a similar size range of 300 to 750 nm, nodular oxides were observed for a normal BWR temperature of 288°C, but a thick uniform oxide was observed for operation at 307°C.

3. For extended–burnup operation, increased precipitation of hydrides and small cubic–ZrO_2 particles, apparently formed via irradiation–induced process, is expected near the metal–oxide boundary, resulting in a more pronounced cracking along the boundary. It is suggested that this may be associated with the accelerated oxidation reported for extended–burnup service ≳ 50 MWd/kgU.

6. ACKNOWLEDGMENT

The author is grateful for the experimental contributions provided by R. A. Conner, Jr. and A. Philippides. This work was supported by the U. S. Department of Energy, under Contract W–31–109–Eng–38.

7. REFERENCES

1. Griffiths, M., Gilbert, R. W., and Cheadle, B. A., Proc. Workshop on Second Phase Particles in Zircaloys, Erlangen, West Germany, June 1985; also issued as AECL–8852.

2. Yang, W. J. S., Tucker, R. P., Cheng, B., and Adamson, R. B., J. Nucl. Mat. 138 (1986) 185–195.

3. Gilbert, R. W., Griffiths, M., and Carpenter, G. I. C., J. Nucl. Mat. 135 (1985) 265–268.

4. Harris, L. L., and Yang, W. J. S., Radiation–induced Changes in Microstructure: 13th International Symposium (Part I), ASTM STP 955, F. A. Garner et al., ed., American Society for Testing and Materials, Philadelphia, 1987, pp. 661–675.

5. Garzarolli, F., Dewes, P., Maussner, G., and Basso, H. H., Proc. Eighth International Symposium on Zirconium in Nuclear Industry, June 19–23, 1988, San Diego, CA, in press.

6. Motta, A. T., and Olander, D. R., "Electron–induced Amphorphization of Precipitates in Zircaloy," in Proc. 14th International Symposium on Effects of Radiation on Materials, June 27–30, 1988, Andover, MA, in press.

7. Bangaru, N. V., Busch, R. A., and Schemel, J. H., in Zirconium in Nuclear Industry: Seventh International Symposium, ASTM STP 939, 1987, pp. 341–363.

8. Grange, J. M., Charquet, D., and Moulin, L., in Zirconium in Nuclear Industry: Fifth Conference, ASTM STP 754, 1982, pp. 96–104.

9. Griffiths, M., Gilbert, R. W., and Carpenter, G. J. C., J. Nucl. Mater. 150 (1987) 53.

10. Chung, H. M., Radiation–induced Changes in Microstructure: 13th International Symposium (Part I), ASTM STP 955, 1987, pp. 676–699.

11. Rudling, P., Vannesjö, K. L., Vesterlund, G., and Massih, A. R., Zirconium in the Nuclear Industry: Seventh International Symposium, ASTM STP 939, 1987, pp. 292–306.

12. Garzarolli, G., and Stehle, H., in Improvements in Water Reactor Fuel Technology and Utilization, Proc. of IAEA Symposium, Stockholm, September 15–19, 1986, pp. 387–407.

13. Chung, H. M., and Kohli, R., unpublished work, 1985.

14. Adamson, R. B., Tucker, R. P., and Fidleris, V., Zirconium in the Nuclear Industry, Fifth Conference, ASTM STP 754, 1982, pp. 208–234.

15. Chung, H. M., and Yaggee, F. L., and Kassner, T. F., Zirconium in the Nuclear Industry: Seventh International Symposium, ASTM STP 939, 1987, pp. 775–801.

16. Johnson, A. B., Jr. Battelle Northwest Laboratory Report BN–SA–1921, 1984.

17. Lanning, D. D., Johnson, A. B., Jr., Trimble, D. J., and Boyd, S. M., Zirconium in Nuclear Industry: Eighth International Symposium, June 19–23, 1988, San Diego, CA, in press.

18. Holzer, R., and Knaab, H., Recent Fuel Performance Experinece and Implementation of Improved Products, in Proc. ANS Topical Meeting on LWR Fuel Performance, April 17–20, 1988, Williamsburg, VA; American Nuclear Society, La Grange Park, IL, pp. 69–80.

19. Quinaux, J. P., et al., AFA Proves Its Worth, Nucl. Eng. International, December 1988, p. 43.

20. Newman, L. W., The Hot Cell Examination of Oconee–1 Fuel Rods after Five Cycles of Irradiation, Babcock and Wilcox, BAW–1874 (DOE/ET/34212–50), October 1986.

21. Andrews, M. G., Smith, G. P., and Shubert, M. A., Experience and Developments with Combustion Engineering Fuel, Proc. ANS Topical Meeting on LWR Fuel Performance, April 17–20, 1988, Williamsburg, VA; American Nuclear Society, La Grange Park, IL (1988), pp. 90–95.

22. Kaiser, R. S., Miller, R. S., Moon, J. E., and Pisano, N. A., "Westinghouse's High Burnup Experience at Farley–1 and Point Beach–2," Proc. ANS Topical Meeting on LWR Fuel Performance, April 17–20, 1988, Williamsburg, VA; American Nuclear Society, La Grange Park, IL (1988), pp. 119–124.

23. Garzarolli, F., et al., "Review of PWR Fuel Rod Waterside Corrosion Behavior," EPRI NP–1472, 1980.

Table 1. Summary of BWR and PWR Fuel and Gadolinia Absorber Rods Examined for Characterization of Cladding Microstructure and Waterside Corrosion

Reactor	Fuel	Burnup (MWd/kgU)	Cladding State	Fluence (10^{21} n cm^{-2}, E > 0.1 MeV)	Oxide Morphology	Oxide Layer Thickness (µm)	Size of Intermetallic Precipitates (nm)
BWR–A	UO_2	14	Annealed	2.2	Nodular	3–45	340–750
BWR–B[1]	UO_2	30	Cold–worked Stress–relieved	3.3	Uniform – thick	50–70	300–600
BWR–C	UO_2	11	Annealed	1.6	Nodular	2–40	320–730
BWR–D[2]	UO_2–3% Gd_2O_3	24	Cold–worked Stress–relieved	3.1	Uniform – thin	5–9	240–480
PWR–A	UO_2	28	Cold–worked Stress–relieved	4.4	Uniform – cracked	20–30	40–100

[1] Coolant outlet temperature 307°C instead of normal BWR temperature of 288°C.

[2] Operating temperature of the gadolina–containing absorber rod was ~240°C.

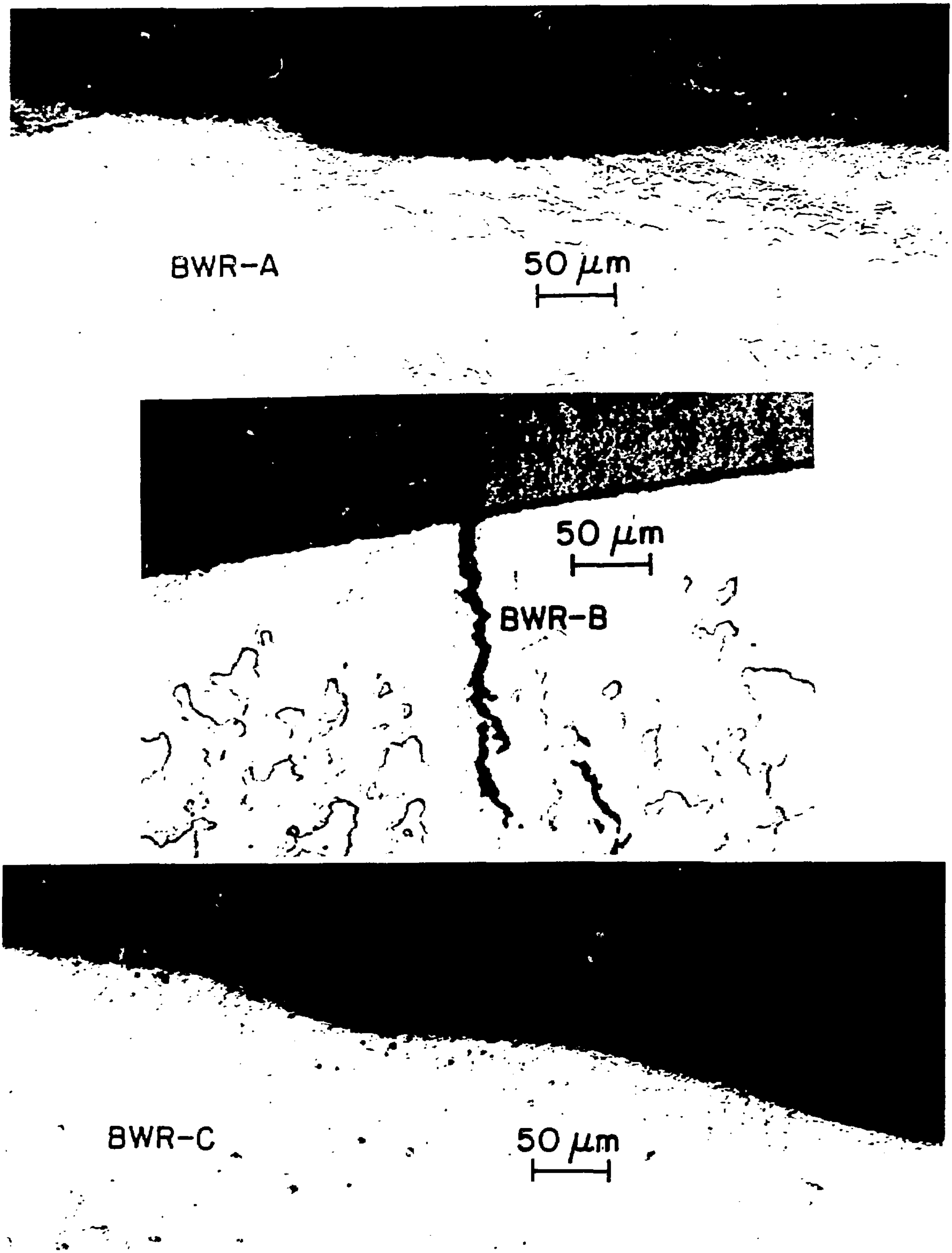

Fig. 1. Morphology and Thickness of Waterside Corrosion Layers of Fuel and Absorber Rods of BWR and PWR after Burnup of 11–30 MWd/kgU.

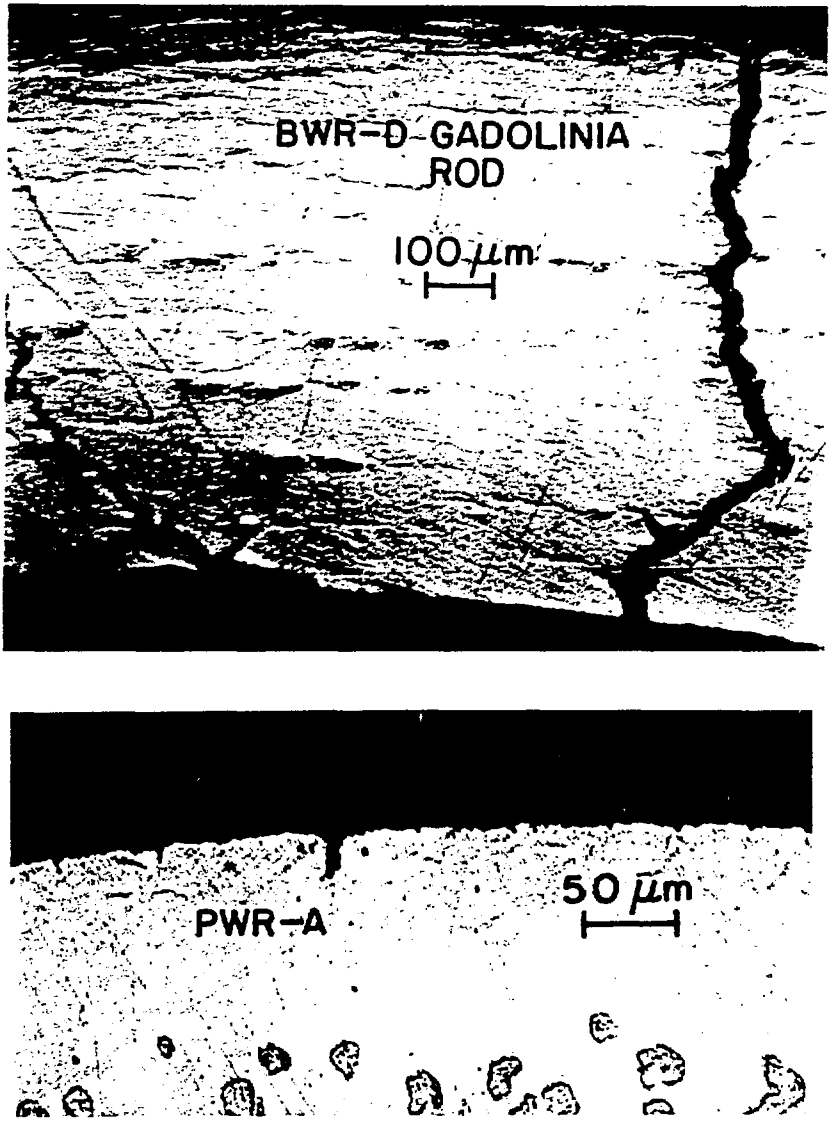

Fig. 1. (Contd.)

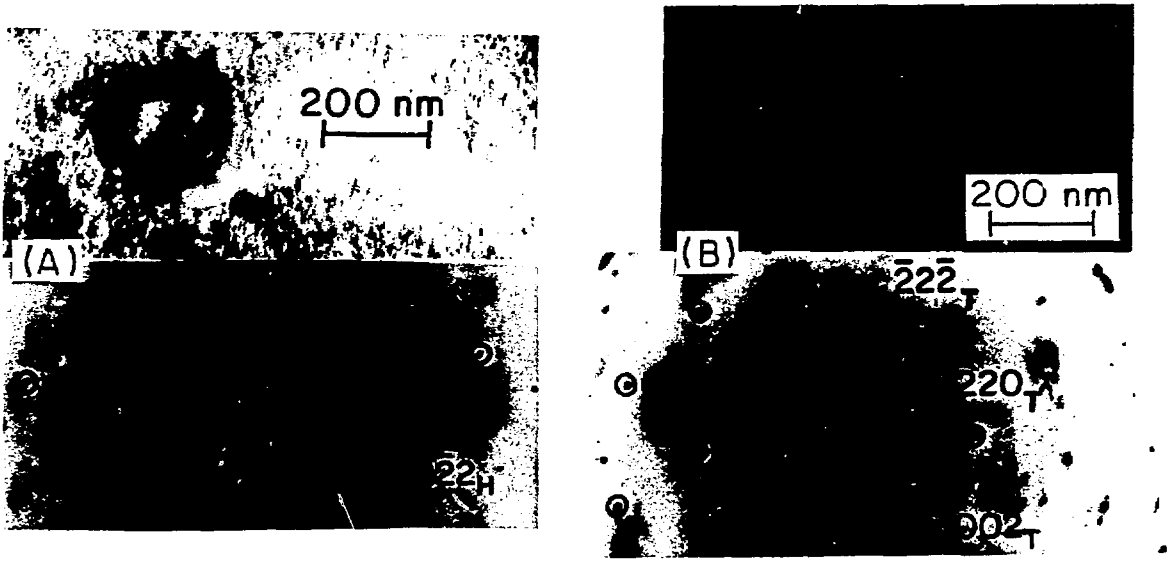

Fig. 2. Morphology and SAD Patterns of Hexagonal Zr(Fe,Cr)$_2$ (A) and Tetragonal Zr$_2$(Fe,Ni) Precipitates (B) Observed in the BWR–B Fuel Cladding after Fluence of 3.3 x 10^{21} ncm^{-2}.

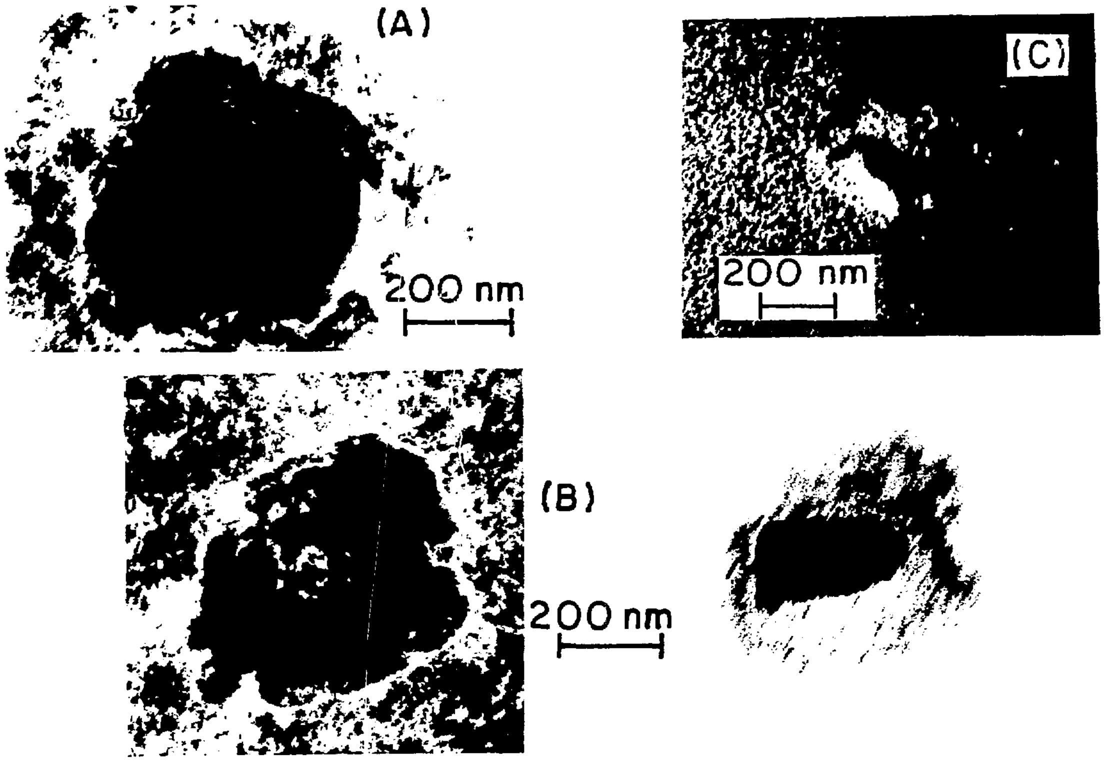

Fig. 3. Morphology of Intermetallic Precipitates in Fuel and Gadolinia Claddings of BWR–A, –C, and –D.

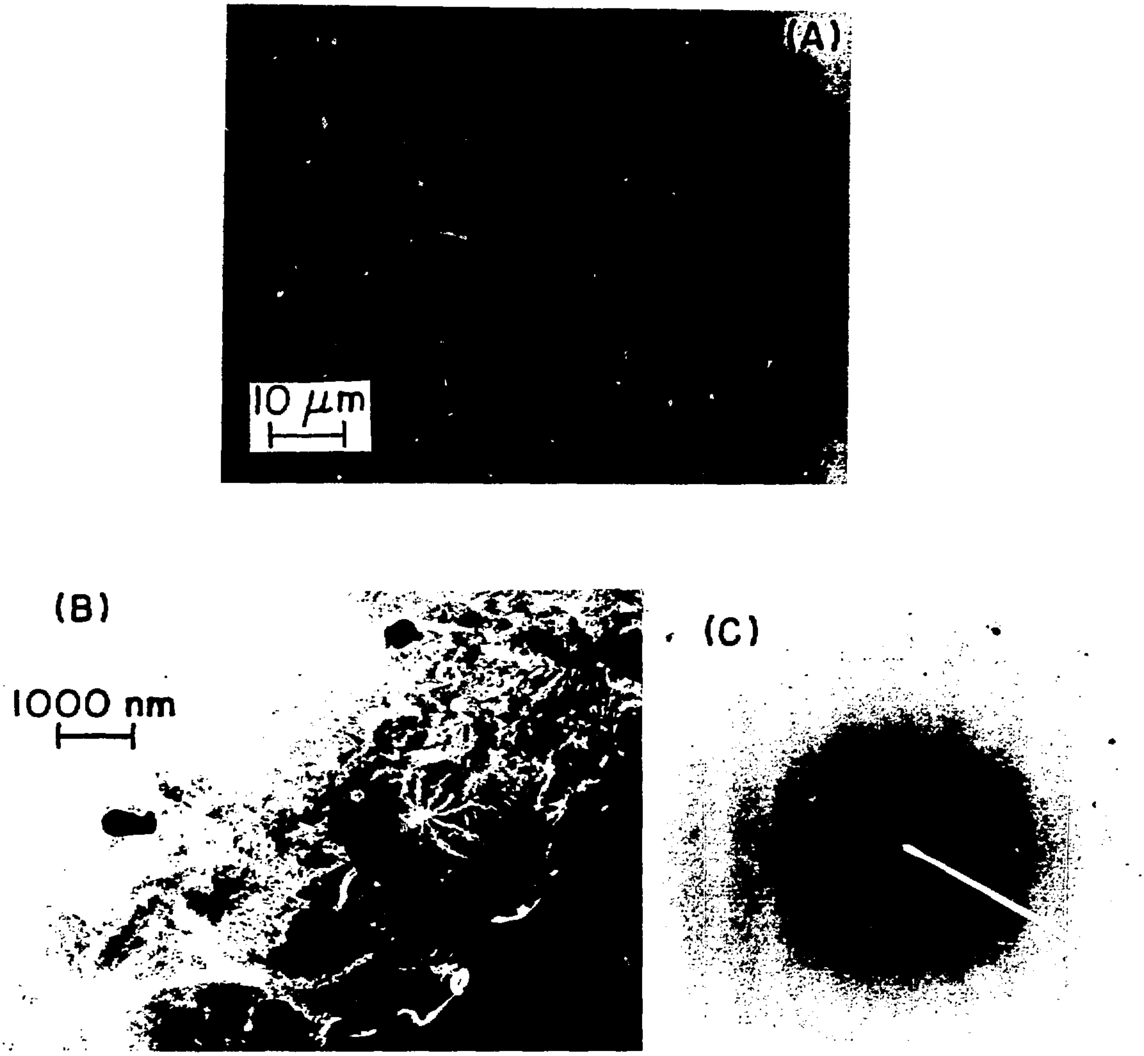

Fig. 4. Distribution (A) and Morphology (B) of Small Holes and Amorphized Local Regions Produced in TEM Specimens of PWR–A Cladding. The holes were produced as a result of preferential localized corrosion attack during jet–thinning near the amorphized and dissolved $Zr(Fe,Cr)_2$ precipitates. Diffraction pattern of the amorphous region is shown in (C).

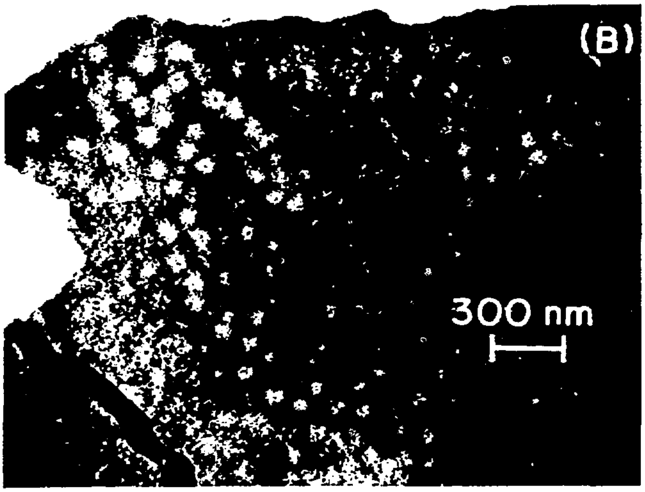

Fig. 5. Alternating Dark and Light Contrasts in a Bright–Field Image of PWR Cladding Indicating an Irradiation–induced Spinodal–like Fluctuation of Local Solute Concentration Following Complete Amorphization and Dissolution of the Intermetallic Precipitates.

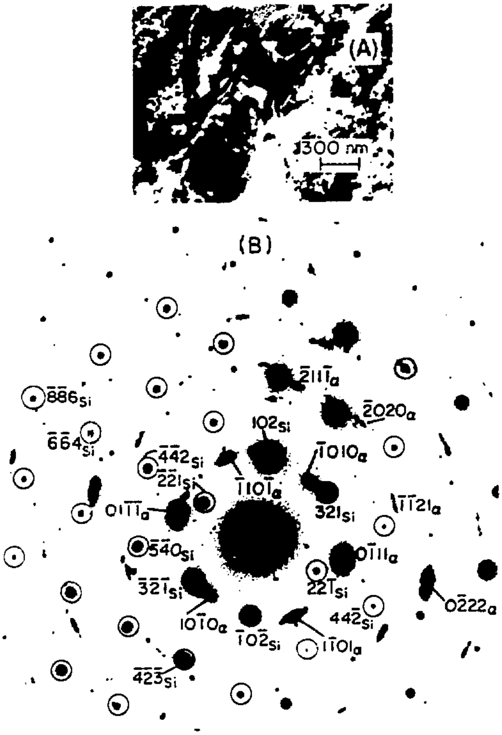

Fig. 6. Bright–Field Image (A) and SAD Pattern (B) of a Zr_3Si Precipitate Observed in Zircaloy–4 of PWR–A.

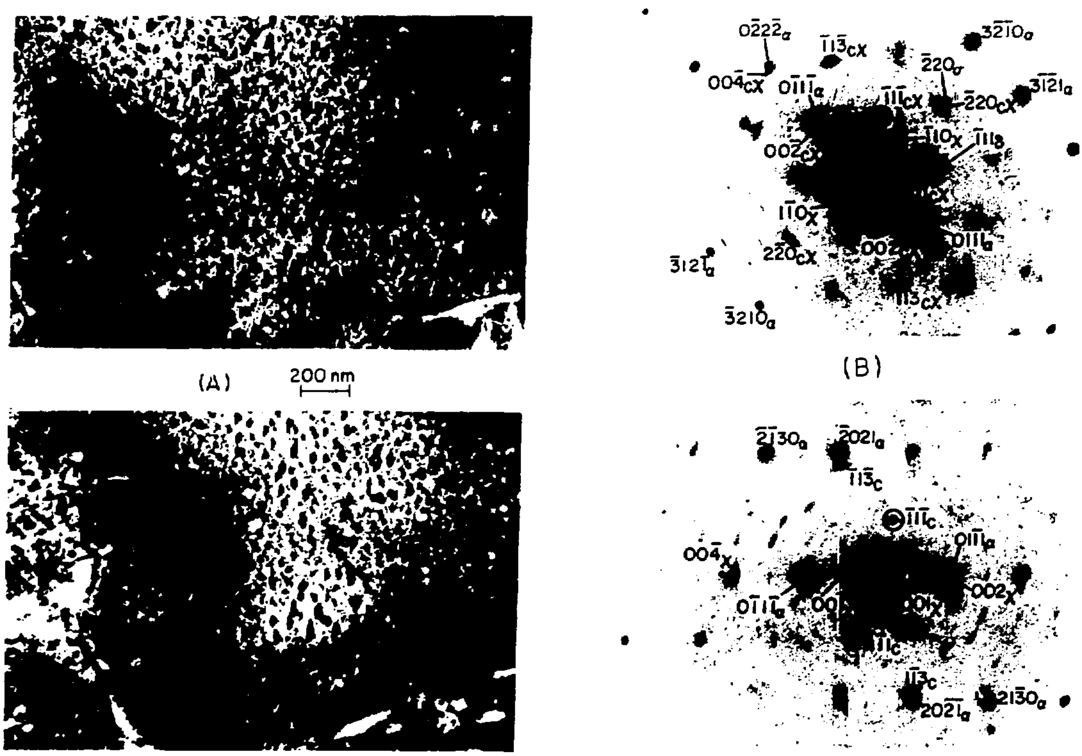

Fig. 7. Stereomicroscopy Analysis of Precipitates Observed in BWR–D Gadolinia Rod Zircaloy–2 Cladding. (A) Bright–field stereopair obtained by 10° tilting; (B) SAD patterns before and after the 10° tilt, showing reflections from α–Zr, cubic–ZrO_2, δ–hydride, and surface artifact hydride, each denoted by letter α, c, δ, and χ; (C) 75 images selected for determination of the relative depth distribution (images near the top, middle, and bottom part of the thin film are denoted by triangles, circles, and squares, respectively); (D) 30 stereopair dark–field images, produced from the $(\bar{1}1\bar{1})$ reflections of cubic–ZrO_2 in (B), selected for measurement of relative depth distribution of the precipitates; (E) relative depth distribution of the 30 selected cubic–ZrO_2 precipitates of (D), showing a more or less random bulk distribution.

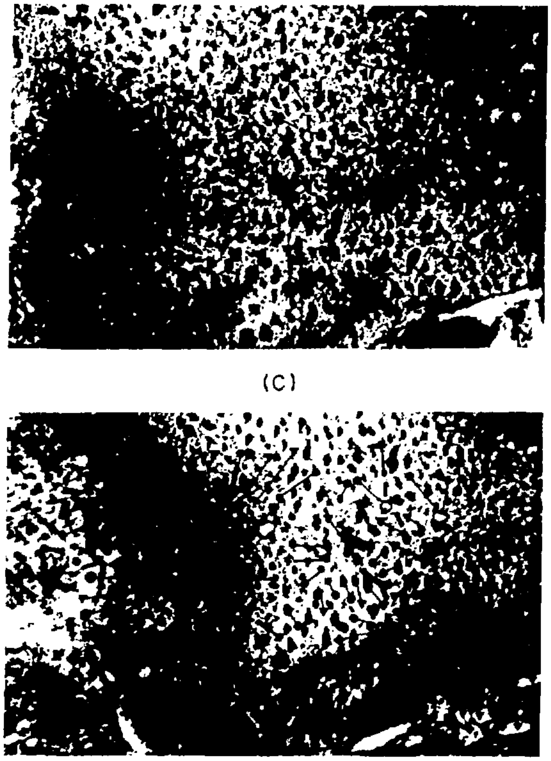
(C)

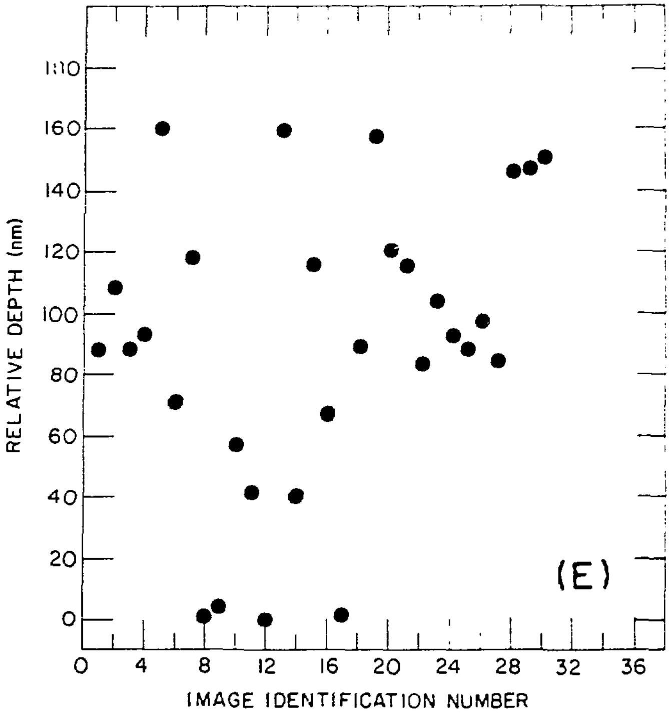
RELATIVE DEPTH (nm)
180
160
140
120
100
80
60
40
20
0
0
4
8
12
16
20
24
28
32
36
IMAGE IDENTIFICATION NUMBER
(E)

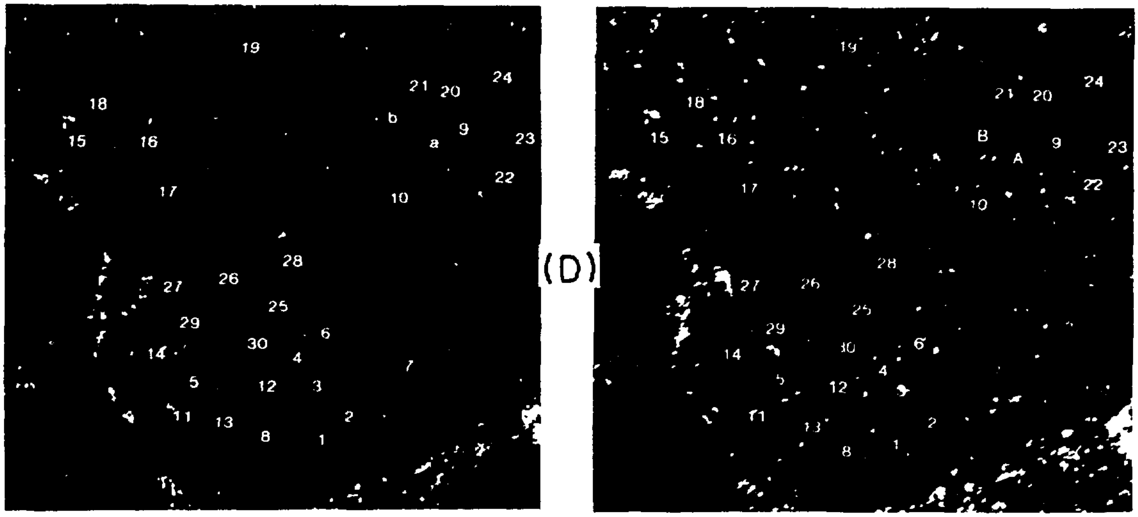
(D)
19
18
21
20
24
15
16
b
a
9
23
22
17
10
28
27
26
25
29
6
14
30
4
7
5
12
3
11
13
2
8
1
B
A

Fig. 7. (Contd.)

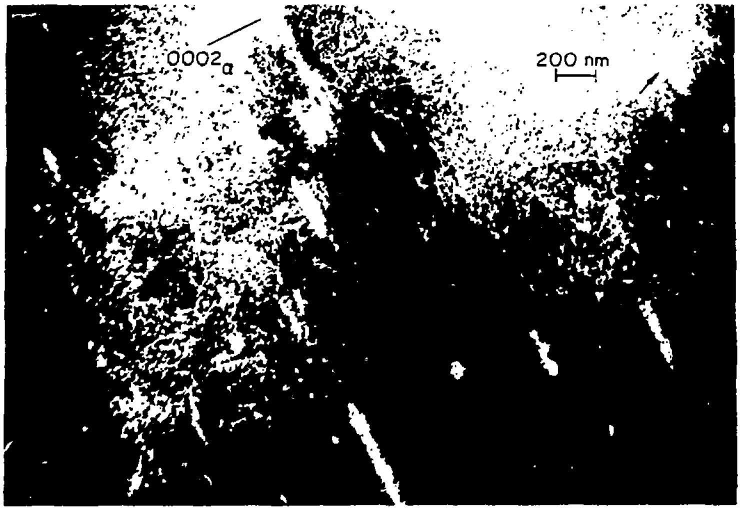

Fig. 8. Dark–Field Image Produced from Reflections of (0002) of Zr, (111) of δ–Hydride, and (002) of Cubic–ZrO_2 Showing Hydride Precipitation in Association with C–Component Dislocations. Hydrides are denoted by arrows.

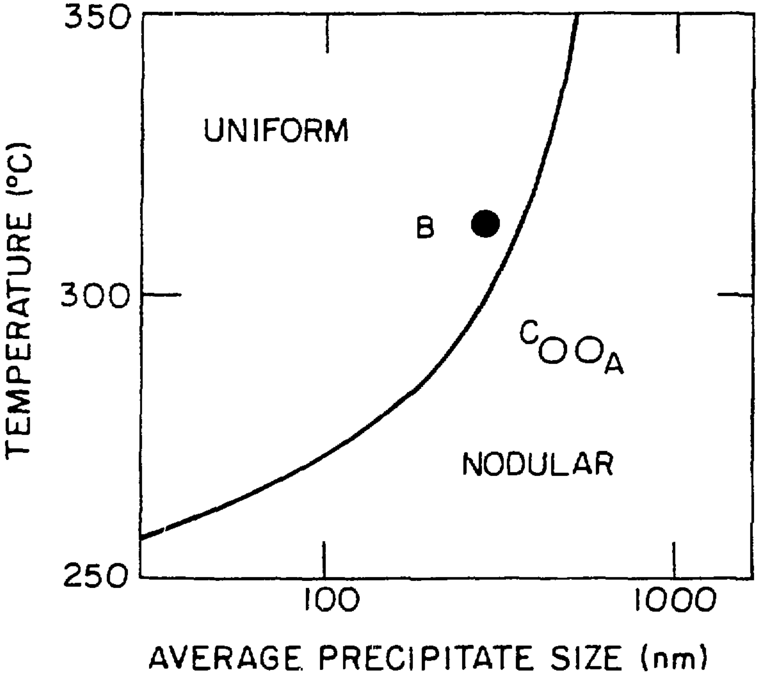

Fig. 9. Schematic Illustration of Expected Occurrence of Uniform and Nodular Oxidation in BWR as a Function of Clad Temperature and Average Size of Intermetallic Precipitates.